Microwave Rabi resonances beyond the small-signal regime

A. Tretiakov[1] and L. J. LeBlanc[1,2,*]

[1]*Department of Physics, University of Alberta, Edmonton, Alberta T6G 2E1, Canada*
[2]*Canadian Institute for Advanced Research, Toronto, Ontario M5G 1M1, Canada*

The coupling between microwave fields and atoms (or atomlike systems) is inherently weaker than for optical fields, making microwave signal manipulation for applications like quantum information processing technically challenging. In order to better understand this coupling and to develop tools for measuring it, we explore the microwave coupling to atoms using the "atomic candle" technique, and push it beyond the bounds of the small-signal regime in order to deliver a larger signal. In familiar two-level systems, responses beyond the usual Rabi oscillations can arise when a single-tone drive is phase modulated, causing the steady-state populations to oscillate at integer harmonics of the modulation frequency. Resonant behavior of the first two harmonics for frequencies near the Rabi frequency, known as α and β Rabi resonances, is widely used for microwave-field magnetometry and as a power standard known as the atomic candle. Here, we explore Rabi resonances beyond the small-signal approximation and report upon experimental observations of higher-order-harmonic population response for microwave hyperfine transitions in cold ^{87}Rb atoms, which we compare to numerical simulations.

I. INTRODUCTION

The control and manipulation of microwave signals with atoms is undergoing a renaissance in the scientific world, moving beyond traditional applications such as providing the definition of the second [1–4], towards precision metrology in direct current (dc) [5] and alternating current (ac) [6] magnetometers, and novel applications for quantum information processing, such as microwave-to-optical transduction of qubits [7–9]. These two examples highlight two different ways atoms are used: first, as a measurement tool to detect the fields, and second, as the interaction medium through which the fields are manipulated. Both cases demand an intimate understanding of the microwave-to-atom coupling, and a way to measure it precisely and with a large signal-to-noise ratio.

Very generally, an oscillating electromagnetic field with a frequency near the resonance of a two-level system periodically drives population transfer between levels, in a process commonly known as Rabi oscillation. In the presence of relaxation between these levels (due to one or more of many possible decoherence mechanisms), the steady-state populations tend towards a constant value. In contrast, these steady-state populations oscillate when the phase of the oscillating field is modulated at a frequency ω_m, and the amplitude of the population oscillations is enhanced when ω_m is equal to the Rabi frequency, Ω_R. This phenomenon, known as "Rabi resonance" [10–12], can be used to find the the system's Rabi frequency and, correspondingly, the power of the oscillating field at the position of the atom(s). The Rabi-flopping atoms respond to ac and dc fields in exactly the same way in all laboratories, so by measuring the rate of flopping we have a fundamental measure of the field strength at the atoms. In analogy to "candlepower," a measure of luminous intensity,

such measurement schemes in Rabi-flopping atomic systems are known as "atomic candles" [12,13] and are used as electromagnetic power standards. This technique has also attracted significant interest for its applications for ac magnetometry inside microwave (MW) cavities [5,14], MW wave guides [15–17], and in free space [5,18–21]. Applying static magnetic fields [14] and using multispecies vapor cells [5] adds frequency tunability and expands the operational bandwidth of this technique.

In previous work, the Rabi resonance was analyzed and measured only in the small-signal regime, where a sufficiently small modulation depth permits an approximate analytic solution to the Maxwell-Bloch equations for the populations. These population oscillations, which have frequency components at ω_m and $2\omega_m$, can be described analytically, including an amplitude that depends on ω_m. Here, we explore the atomic candle technique beyond the small-signal approximation both numerically and experimentally. Using large-deviation phase modulation on the MW field, we observe higher-order spectral features whose characteristics and scaling behave differently than the first and second harmonics. In this work, we focus our attention on the component oscillating at $4\omega_m$, namely, the fourth harmonic, and discuss how it may be used to extend the atomic candle technique.

II. THEORY: RABI OSCILLATIONS WITH A PHASE-MODULATED DRIVING FIELD

As we explore higher-order Rabi resonances theoretically, we consider the two-level system used in our experiments (Fig. 1), which is comprised of two Zeeman states in different hyperfine levels of an alkali metal, which are described by the total angular momentum F and projections m_F. For this two-level system, separated by energy $\hbar\omega_0$, the levels can be coupled by a nonzero matrix element for magnetic dipole transitions, $V_{12} = \langle 2| \hat{\boldsymbol{\mu}} \cdot \mathbf{B}_0 |1\rangle$, where $\hat{\boldsymbol{\mu}}$ is the magnetic dipole

_____
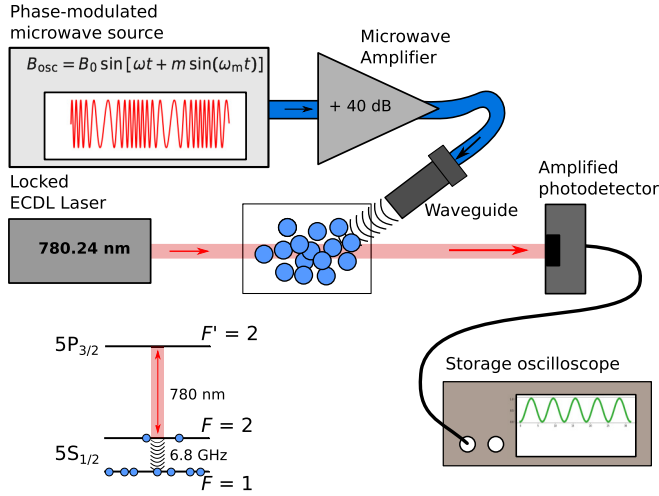*Corresponding author: lindsay.leblanc@ualberta.ca

FIG. 1. Schematic of phase-modulated microwave signals applied and measured in an atomic system, as used in experimental demonstrations. After optical molasses ^{87}Rb atoms are optically pumped into the $F = 1$ state transparent for a probe light, resonant with the $F = 2 \rightarrow F' = 2$ transition. Change in the $F = 2$ population due to microwave field is monitored in real time as a change in transmission signal of the probe light.
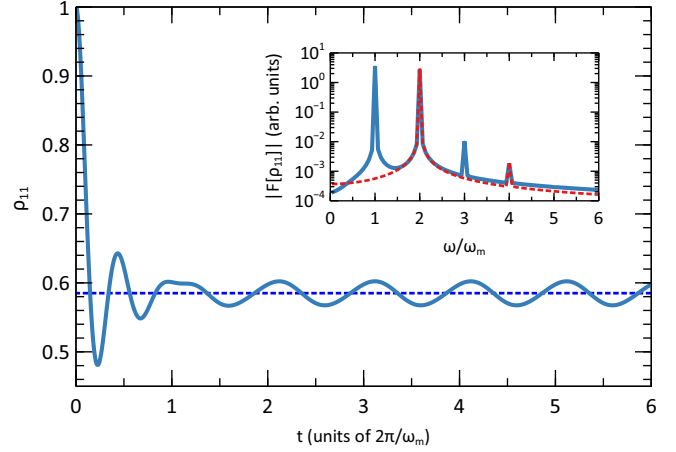

FIG. 2. Ground-state population of a two-level system as a function of time in the case of a phase-modulated coupling (solid line). The simulation is made for modulation depth $m = 1$, Rabi frequency $\Omega_R = 2\omega_m$, longitudinal and transverse relaxation rates $\Gamma_1 = 0.8\omega_m$ and $\Gamma_2 = 0.4\omega_m$, respectively, and carrier frequency detuning $\delta = \omega_m$, where ω_m is the modulation frequency. The dashed curve corresponds to the steady-state solution without modulation. Inset: Spectrum of the steady-state oscillations in the ground-state population for $\delta = 0.1\omega_m$ (blue solid curve) and $\delta = 0$ (red dashed curve), obtained using fast Fourier transform (FFT).

operator, and $|1\rangle$ and $|2\rangle$ represent the two levels. Here, the ac driving field $\mathbf{B}(t) = B_0\mathbf{e}_{B0}\cos\omega t$ is described by the peak field $\mathbf{B}_0 = B_0\mathbf{e}_{B0}$, with ac-field amplitude B_0 and direction $\mathbf{e}_{B0}$. When the ac field is resonant ($\omega = \omega_0$), the population oscillates at the Rabi frequency $\Omega_R = V_{12}/\hbar$. When the detuning $\delta = \omega - \omega_0$ is nonzero, the oscillations occur at the generalized Rabi frequency $\Omega = \sqrt{\Omega_R^2 + \delta^2}$.

In the presence of decoherence or damping, the oscillatory behavior of the two-level system damps out and the system equilibrates to a steady population ratio (e.g., equal populations for a strong resonant ac field and small damping). These dynamics are well described by the Maxwell-Bloch equations [22].

A phase-modulated oscillating field changes these dynamics. Here, we consider the case where a time-dependent phase $\theta(t)$ modulates the ac field: $\mathbf{B}(t) = B_0\mathbf{e}_{B0}\cos[\omega t + \theta(t)]$. In this case, the standard Maxwell-Bloch equations can be modified to include additional time-dependent terms:

$$\dot{u} = [\delta + \dot{\theta}(t)]v - \Gamma_2 u, \tag{1}$$

$$\dot{v} = -[\delta + \dot{\theta}(t)]u + \Omega_R w - \Gamma_2 v, \tag{2}$$

$$\dot{w} = -\Omega_R v - \Gamma_1[w + 1], \tag{3}$$

where u and v are the in- and out-of-phase coherences [$u = 2\text{Re}(\rho_{12})$ and $v = 2\text{Im}(\rho_{12})$] and $w = \rho_{22} - \rho_{11}$ is the population difference between levels, and where ρ is the usual 2×2 density matrix of the two-level system (ρ_{11} is the ground-state population and ρ_{22} is the excited-state population). In the loss terms, Γ_1 and Γ_2 represent longitudinal and transverse damping rates, respectively. We consider the case where the ac field is modulated about a constant phase offset θ_0 with frequency ω_m, modulation depth m, and offset phase ϕ_m:

$$\theta(t) = \theta_0 + m\sin(\omega_m t + \phi_m). \tag{4}$$

We explore the numerical solutions of Eqs. (1)–(3) to find the time-dependent coherences and population dynamics under a variety of parameters. In particular, we are interested in the excited-state population $\rho_{22} = (w + 1)/2$ in the steady-state regime ($\Gamma_1 t \gg 1$), which is found to oscillate, even long after the damping times associated with Γ_1 and Γ_2 (Fig. 2).

Below, we have a closer look at the time dependence of the steady-state populations of the ground and excited states, which is directly related to a measurable quantity: the absorption of light from one of these levels to an optically excitable third level.

A. Small-modulation approximation

Treating the modulation term as a perturbation allows us to assume that in the steady-state regime the parameters describing the atomic state evolve around their unmodulated steady-state values u_0, v_0, $\rho_{22,0}$:

$$\rho_{22}(t) = \rho_{22,0} + \rho_{22,m}(t),$$

$$v(t) = v_0 + v_m(t),$$

$$u(t) = u_0 + u_m(t),$$

where $\rho_{22,m}$, v_m, u_m describe the evolution due to the phase modulation.

Figure 2 shows that in the case of a weak modulation, the steady-state ground-state population $\rho_{11}(t)$ oscillates around its unmodulated value. Indeed, it can be shown [13] that in this case the excited-state population evolution is described by

$$\ddot{\rho}_{22,m} + \Gamma_1\dot{\rho}_{22,m} + \Omega_R^2\rho_{22,m}$$
$$= 2\Omega_R\Gamma_2 v_m + 2\Omega_R(\delta + \dot{\theta})u_m + u_0\Omega_R\dot{\theta},$$

which is a damped harmonic oscillator equation, where the driving is due to coherence between the levels (v_m and u_m) and phase modulation $\dot{\theta}$.

For small modulations ($m < \sqrt{2\Gamma_1/\omega_m}$) and low decoherence ($\Gamma_2 \ll \omega_m$), known as the small-signal approximation, the steady-state solution for the excited-state population has been found analytically [13]. The population dynamics in this regime are represented by the first two harmonics of ω_m, and the excited-state dynamics with respect to its unperturbed value may be expressed as

$$\rho_{22,m}(t) = P_1 \sin(\omega_m t + \phi_1) + P_2 \sin(2\omega_m t + \phi_2), \quad (5)$$

with amplitudes

$$P_1 = \frac{\frac{m}{2}\omega_m\Omega_R^2\delta}{\left[\Gamma_2^2 + \delta^2 + \frac{\Gamma_2}{\Gamma_1}\Omega_R^2\right]\sqrt{\left(\omega_m^2 - \Omega_R^2\right)^2 + \Gamma_1^2\omega_m^2}}, \quad (6)$$

$$P_2 = \frac{\left(\frac{m}{2}\right)^2\omega_m\Omega_R^2\Gamma_2}{\left[\Gamma_2^2 + \delta^2 + \frac{\Gamma_2}{\Gamma_1}\Omega_R^2\right]\sqrt{\left(4\omega_m^2 - \Omega_R^2\right)^2 + 4\Gamma_1^2\omega_m^2}}. \quad (7)$$

The main feature of these solutions is that the amplitudes $P_1(\omega_m, \Omega_R)$ and $P_2(\omega_m, \Omega_R)$ peak when the frequency of the corresponding harmonic is resonant with the Rabi frequency, $\omega_m = \Omega_R$ and $2\omega_m = \Omega_R$, respectively, which are known as the α and β Rabi resonances. Experimentally, scanning the modulation frequency ω_m in search of this peak provides a tool for measuring Ω_R and, thus, the power of the driving field, since $\Omega_R \propto B_0^2$ [5]. In addition, the amplitude of the first harmonic disappears at zero carrier detuning, $\delta = 0$ ($P_1 \propto \delta$). By tuning the carrier frequency ω to field-sensitive transitions [5], this dependence provides a means by which to measure static magnetic fields.

The inset of Fig. 2 compares the spectra of the steady-state ρ_{11}, simulated for $\delta = 0$ and $\delta = 0.1\omega_m$. As is expected, the first harmonic vanishes at zero carrier detuning. In the simulation, the magnitudes of the decoherence rates are comparable with the modulation frequency, which violates the small-signal approximation and leads to additional oscillations at third and fourth harmonics, even though their amplitudes are a few orders of magnitude smaller than P_1 and P_2.

B. Large modulation: Numerical analysis

A general solution of the phase-modulated oscillatory dynamics of a two-level system, with arbitrary phase and amplitude modulation, was obtained in Ref. [23].

Still, there is no simple analytical expression for the case where the phase is modulated according to Eq. (4). Numerical simulations of the large-modulation condition (Fig. 3) show that the steady-state ground-state population has a periodic solution, but, unlike in the small-modulation case, its average is shifted from the unmodulated value and its spectrum consists of many harmonics at multiples of ω_m:

$$\rho_{11}(t) = \sum_n P_n \sin(n\omega_m t + \phi_n),$$

where n can be any positive integer and ϕ_n is the phase of the response. As might be expected from small-signal theory, the relative height of the spectral constituents P_n depends on m, ω_m, Ω_R, $\Gamma_{1,2}$, and δ. In the case when $\delta = 0$, all *odd*
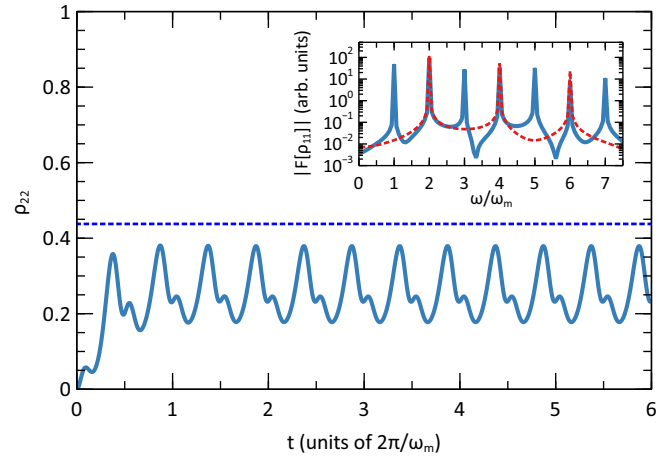

FIG. 3. Excited-state population of a two-level system as a function of time in the case of a phase-modulated coupling (solid line) with $m = 6$ rad, $\Omega_R = 1.5\omega_m$, $\Gamma_1 = 0.8\omega_m$, $\Gamma_2 = 0.4\omega_m$, and $\delta = 0$. The dashed line corresponds to the steady-state solution without modulation. Inset: Spectrum of the steady-state oscillations in the excited-state population for $\delta = \omega_m$ (blue solid curve) and $\delta = 0$ (red dashed curve).

components disappear, which is consistent with the analytical small-signal solutions [Eq. (5)]. However, compared to the small-signal solution, the large-modulation dynamics include additional spectral peaks, and thus more (correlated) information from which to extract the field calibration, providing more options for extracting the final results.

Next, we evaluate the response of the excited-state population when the carrier frequency is equal to the frequency of the transition between the ground and excited states (i.e., $\delta = 0$), which is the regime of practical interest. Here, the ground-state population's response to phase modulation includes only the even harmonics of ω_m and we study, in particular, the second and fourth harmonics for different values of the modulation index m. We are interested only in the steady-state response, where $\Gamma_1 t_1 \gg 1$ and any "normal" Rabi oscillations would have damped out.

To extract values of the spectral amplitudes P_n of the steady-state ground-state population signal $\rho_{11}(t)$ from our numerical simulations, we consider both the in- and out-of-phase responses of the signal at frequency $n\omega_m$:

$$a_n = \frac{1}{N}\sum_{k=1}^{N}\rho_{11}(t_k)\sin n\omega_m t_k,$$

$$b_n = \frac{1}{N}\sum_{k=1}^{N}\rho_{11}(t_k)\cos n\omega_m t_k,$$

where the t_k represent the evenly spaced discrete time points, and the index k runs over all time indices. This approach to the analysis provides the amplitudes of the components at each harmonic of the modulation frequency ω_m, and the overall amplitude is given by $P_n = 2\sqrt{a_n^2 + b_n^2}$.

This analysis relies on the fact that a_n and b_n approach zero as N approaches infinity for any frequency other than the reference frequency (i.e., $\omega \neq n\omega_m$). In the case when N is finite, the contribution from these unwanted frequencies can
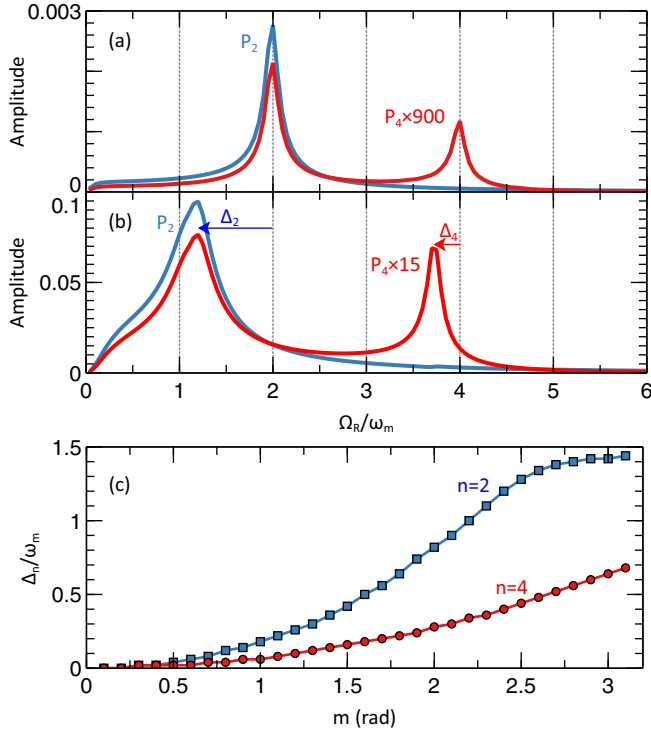
FIG. 4. Rabi resonances for amplitudes of (a) second (P_2) and (b) fourth (P_4) harmonics for $m = 0.25$ rad and $m = 2$ rad, respectively. The amplitude of the fourth harmonic is scaled for better visibility, as indicated. At higher m peaks shift with respect to their original positions $\Omega_R = 2\omega$ and $\Omega_R = 4\omega$, which is indicated by Δ_2 and Δ_4, respectively. (c) Shifts of the Rabi resonance peaks with respect to their weak-modulation positions as a function of the modulation index. Simulation is made for $\Gamma_1 = 2\Gamma_2 = 0.08\omega_m$ and $\delta = 0$.

be significant, so we filter them out in the frequency domain using fast Fourier transform and its inverse. To reduce the contribution of the numerical artifacts due to finite duration of the analyzed signal, we apply a Hamming window to $\rho_{11}(t)$ before calculating a_n and b_n.

1. Rabi resonance: Low decoherence rate

Figure 4(a) shows the simulated amplitude response for the second and fourth harmonics as a function of the Rabi frequency with fixed ω_m and $\Gamma_1, \Gamma_2 \ll \omega_m$. In agreement with Eq. (7), the amplitude P_2 of the second harmonic peaks when $\Omega_R = 2\omega_m$. The fourth harmonic has two resonances: at $\Omega_R = 2\omega_m$ and $\Omega_R = 4\omega_m$. The latter peak is similar to the frequency response of a damped harmonic oscillator whose natural frequency is Ω_R and is driven harmonically at $4\omega_m$. In contrast, the resonant behavior of the second and fourth harmonics in the case of large phase modulation deviates from this small-signal approximation, as seen in Fig. 4(b). Both harmonics' resonance peaks shift toward smaller values of Ω_R/ω_m, but the shift of P_2's peak (i.e., Δ_2) is much more significant than that of P_4 (i.e., Δ_4). Additionally, its shape changes drastically, including an increase in the linewidth. The value of this shift as a function of m is shown in Fig. 4(c),
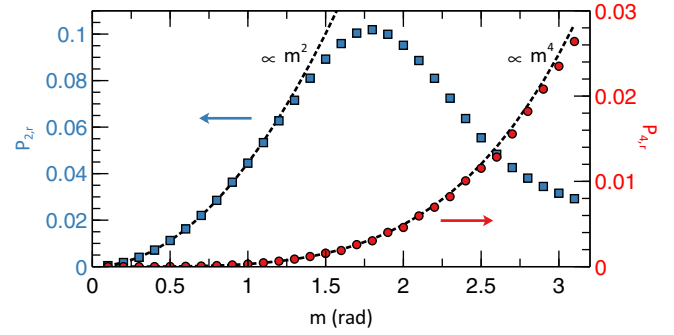

FIG. 5. Height of the Rabi resonance peaks of second (blue squares) and fourth harmonic (red circles) as a function of modulation depth, determined from numerical simulation with $\Gamma_1 = 2\Gamma_2 = 0.08\omega_m$ and $\delta = 0$. The value for fourth harmonic ($P_{4,r}$) is calculated for the right-hand peak in Figs. 4(a) and 4(b), which corresponds to $\Omega_R \approx 4\omega_m$. Black dashed curves correspond to quadratic and quartic functions normalized to $P_{2,r}(m = 1)$ and $P_{4,r}(m = 1)$, respectively, to indicate the corresponding power dependence $P_{2,r}$ and $P_{2,r}$ at lower m.

which indicates that the fourth-harmonic Rabi resonance is more stable against variation of the modulation depth.

Furthermore, the height $P_{4,r}$ of the fourth-harmonic Rabi-resonance peak corresponding to $\Omega_R = 4\omega_m$ scales as m^4, compared to quadratic (m^2) dependence of the second harmonic's peak value $P_{2,r}$ (Fig. 5) [note that the quadratic behavior also fails at large m, indicating that Eq. (7) is no longer valid]. Therefore, in the large-phase-modulation regime, P_4's peak is comparable to that of P_2, and thus it may become advantageous to use a fourth-harmonic atomic candle (4HAC), where the Rabi resonance of the fourth harmonic is used.

2. Rabi resonance: High decoherence rate

According to Eq. (7), the width of the P_2 peak should increase with increasing decoherence rates $\Gamma_{1,2}$. Figure 6 shows that this applies to both P_4 peaks as well, and when
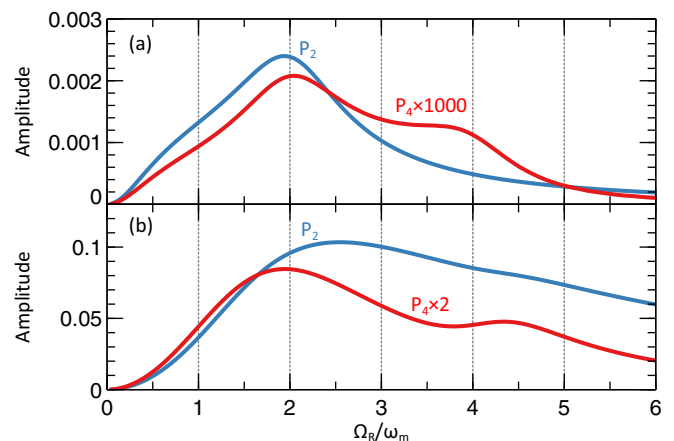

FIG. 6. Rabi resonances for second and fourth harmonics in the case of large decoherence: (a) $m = 0.25$ rad and (b) $m = 6$ rad. Simulation is made for $\Gamma_1 = 2\Gamma_2 = 0.8\omega_m$ and $\delta = 0$. The amplitude of the fourth harmonic is scaled for better visibility.
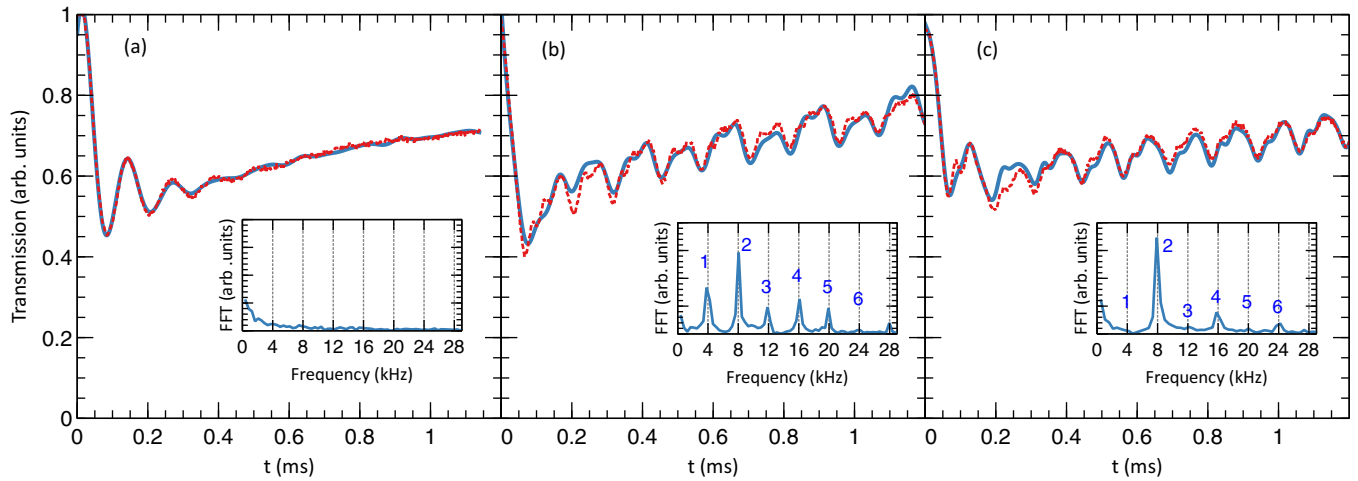
FIG. 7. Typical DR signal for Rabi oscillations as a function of time with a fit according to the model described in the text (red dashed line) and an FFT spectrum of the tail of the signal (inset) for various parameters of the driving MW field. (a) Unmodulated oscillations; (b) $\omega_m/2\pi = 4$ kHz, $m = 2\pi$, $\delta/2\pi = 7$ kHz; (c) $\omega_m/2\pi = 4$ kHz, $m = 2\pi$, $\delta \approx 0$. Axes in all insets have the same scaling. (b) In general, in the case of a phase-modulated driving field the steady-state contains harmonics of the modulation frequency (4 kHz), compared to a flat spectrum in the case of an unmodulated driving field. From (c), it is seen that the odd harmonics disappear when the carrier frequency of the driving field is resonant with the transition. The integer numbers next to peaks in the insets indicate harmonics of ω_m the peaks correspond to. For clarity, only the first 1.5 ms of the DR signal is shown. The probe's power is 46 μW.

the decoherence rate is comparable to ω_m, these two peaks overlap. Even at small m, the P_2 peak's shape is different from a Lorentzian (as in Fig. 4), which indicates that Eq. (7) is no longer valid. For stronger modulation, line broadening and asymmetry make both features unviable for practical applications.

III. EXPERIMENT

A. Experimental setup

To verify the findings of our numerical calculations, we tested the 4HAC technique using our cold-atom apparatus (Fig. 1).

In our experiment we use a cloud of laser-cooled ^{87}Rb atoms, which have undergone standard magneto-optical trapping, followed by an "optical molasses" step giving a 1-mm-wide cloud with typical atom number of 10^8 and temperature of 70 μK. The atoms are optically pumped into the $F = 1$ ground state by switching off the repumping light 1 ms before the cooling and trapping beams are turned off and the atoms begin to expand in time of flight. Next, the cloud is illuminated by a traveling MW field emitted from an open-ended rectangular waveguide, whose phase is modulated periodically with frequency ω_m using built-in functions of the MW source (SRS SG384). The near-resonant MW field (with carrier frequency $\omega/2\pi \approx 6.8$ GHz) transfers the population between the ground states $F = 1$ and $F = 2$. This transfer is observed by monitoring the absorption of a weak probe laser beam resonant with $F = 2 \rightarrow F' = 2$ transition (Fig. 1), which is proportional to the population of state $F = 2$. Since the best signal is produced when both the optical and MW fields are on resonance with the corresponding transitions, this technique is known as the double resonance (DR) [1]. The transmission signal is measured by a high-sensitivity photodetector and recorded with an oscilloscope. During the

laser trapping and cooling stages, the MW source is detuned by $\delta/2\pi = 100$ MHz from the hyperfine splitting, but during the DR interrogation it is quickly brought back to resonance by mixing with an external 100-MHz radio-frequency signal. The MW signal is amplified by a separate amplifier, providing about 2 W of power to the waveguide.

To measure the response of the atoms to the modulated microwave fields, and to test the 4HAC technique, we systematically varied the carrier detuning δ to find the resonant condition. Next, once resonance was found ($\delta = 0$), the phase-modulation frequency was varied to find the Rabi-resonance condition $\delta_m = 0$. The time-dependent transmission of the resonant optical beam served as a measure of the population in the $F = 1$ ground state, and a frequency analysis of the transmission dynamics was performed numerically following the data acquisition.

B. Results and analysis

Using large modulation depths, phase-modulated MW signals applied to our cold atomic samples revealed the multi-harmonic nature of the steady oscillations beyond the small-signal regime. Figure 7 shows the first 1.2 ms of the measured transmission signals (total duration is 5 ms) and derived spectra for three different conditions in our atomic candle experiments. First, we demonstrate "pure" Rabi oscillations [Fig. 7(a)] by applying a resonant but unmodulated MW field. The spectrum here is featureless. Next, when the MW field is strongly modulated but detuned from the hyperfine transition ($m = 2\pi$, $\delta \neq 0$), the population and thus the transmission signal have additional modulations [Fig. 7(b)], and the spectrum contains peaks at integer values of ω_m. Finally, when the carrier frequency is resonant ($\delta = 0$), the odd harmonics of the frequency of the phase modulation are suppressed in the transmission signal [Fig. 7(c)]. We observed that the amplitudes

of the spectral components slightly varied from shot to shot under constant parameters of the MW field setup, and during some of the shots we do not see the total elimination of the odd harmonics. This might be due to noise in the response of the radio-frequency mixer, and for later analysis of the amplitudes we take average values over a few trials.

Because our experiment allows us to record only a very limited number of oscillations in the time domain, spectral analysis using numerical FFTs does not yield a consistent set of results. Instead, we retrieve the spectral information by using the same numerical routine as in Sec. II B. To demonstrate that the steady-state dynamics driven by a phase-modulated field can be qualitatively interpreted as a damped oscillator with natural frequency Ω_R driven at multiples of ω_m, we fit the time-series of the transmission signal $f(t)$ to a model

$$f(t) = \sqrt{A^2 + (Bt)^2} + C_1 e^{-\Gamma_1 t} + C_2 e^{-\Gamma_2 t} \sin^2\left(\frac{\Omega_R}{2}t + \phi\right)$$

$$+ \sum_{n=1}^{6} P_n \sin(n\omega_m t + \phi_n),$$

where the first term accounts for the loss of atoms due to interaction with the probe, the second term accounts for longitudinal damping, the third describes damped Rabi oscillations, and the final terms correspond to the population dynamics at the harmonics of the modulation frequency. In this model, A, B, $C_{1,2}$, P_n, ϕ, and ϕ_n are all fit parameters, where A represents the initial density of atoms at the position of the probe; B is the rate of hole burning due to momentum kicks from the probe; C_1 and C_2 the amplitude of the transmission oscillations, which are proportional to the amplitude oscillations; ϕ and ϕ_n represent the initial phase of the carrier and modulation frequencies at the start of the transmission measurement; and P_n are the steady-state amplitudes of the population oscillation components that we are looking for in this atomic candle measurement.

To investigate practicability of the 4HAC, we analyzed the amplitudes of the second and fourth harmonics, P_2 and P_4, as a function of the modulation frequency ω_m at a fixed MW power. (For these analyses, we use only the tail of the data, which corresponds to the steady-state regime.) Figure 8 shows that the amplitudes of both harmonics peak as ω_m is scanned through $\Omega_R/2 = 2\pi \times (3.8 \pm 0.3)$ kHz in a manner similar to Fig. 6(b), where Ω_R was estimated from an analysis of a set of unmodulated signals. The uncertainty in Ω_R is largely of the same origin as the uncertainties in the amplitudes (as was discussed before), since when the carrier wave is not exactly on resonance with the transition, the oscillation response is at a higher frequency. By fitting a set of transmission data corresponding to the unmodulated driving field, we estimate the decoherence rates in our experiment to be $\Gamma_1 = (2.0 \pm 0.1) \times 10^4$ s^{-1} and $\Gamma_2 = (0.97 \pm 0.04) \times 10^4$ s^{-1}. Even though in this regime Rabi resonances are not practically useful, the qualitative behavior supports our model in numerical analysis.

C. Experimental considerations

In Ref. [13] it was shown that increasing the probe's power leads to a broadening of the line shapes of the atomic-candle Rabi resonances. The absorption and subsequent spontaneous
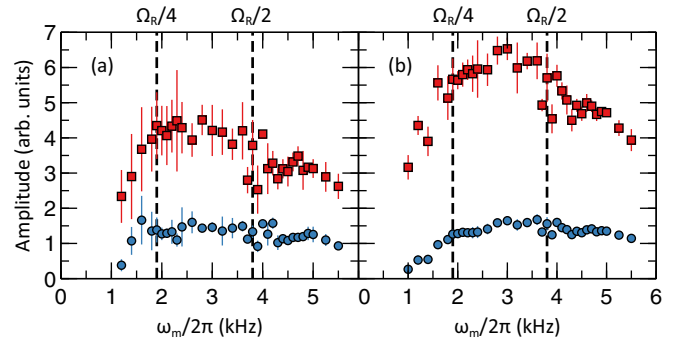

FIG. 8. Rabi resonance features of the second (red squares) and fourth (blues circles) harmonics for $m = 2\pi$, $\delta = 0$ and the probe's power of 46 μW. Each point and its error bar correspond to an average and variance of five values extracted from a tail of a DR signal, respectively. (a) Amplitudes were found by using a quadrature detection discussed in Sec. II B. (b) Amplitudes were found by fitting the DR signal to a model described in Sec. III B. Two vertical dashed lines correspond to $\omega_m = \Omega_R/4$ and $\omega_m = \Omega_R/2$.

emission of a photon by the atom from the upper ground state contributes to the longitudinal relaxation, and thus Γ_1 is proportional to the absorption rate, which in turn is proportional to the probe's intensity.

In our experiment we can observe a similar effect, where by varying the power of the probe beam we can obtain qualitatively different oscillation patterns. Figure 9 shows that increased probe power leads to a higher decoherence rate and changing it by a factor of 10 from 0.54 to 0.06 μW brings the system from highly damped [Fig. 9(a)] to underdamped [Fig. 9(b)] oscillations. This is in a good qualitative agreement with our simulations, where the damped case corresponds to Fig. 3, and a simulation of the underdamped case is shown in Fig. 9(c). Since our simulation model is based on the atom as a two-level system and does not describe the absorption of the probe, it does not capture the monotonically increasing transmission over time that is experimentally observed in the case of the higher probe power. The fact that the average transmission level does not change significantly in the case of the smaller probe intensity indicates that the nonzero steady-state slope of the transmission signal is due to the hole burning in the cloud rather than thermal expansion.

For our steady-state analysis, we want to work in a regime where the Rabi oscillations are damped. Since in our case the interrogation time is limited, this can be achieved by using a higher probe power, corresponding to a strongly damped regime. In addition, higher probe power gives a better signal-to-noise ratio.

The main limitation in our experiment was the short interrogation time, limited by thermal expansion of the atomic cloud and interaction with the probe beam, which was "burning" a hole in the cloud. In addition, we observed slight discrepancies between several successive measurements of the DR signal at constant MW field parameters, which are probably due to fluctuations in the turn-on time of the field. These should not be an issue in the real-world configurations, such as vapor cells, where interaction with the buffer gas keeps the atoms in place, or in cold atoms whose interrogation
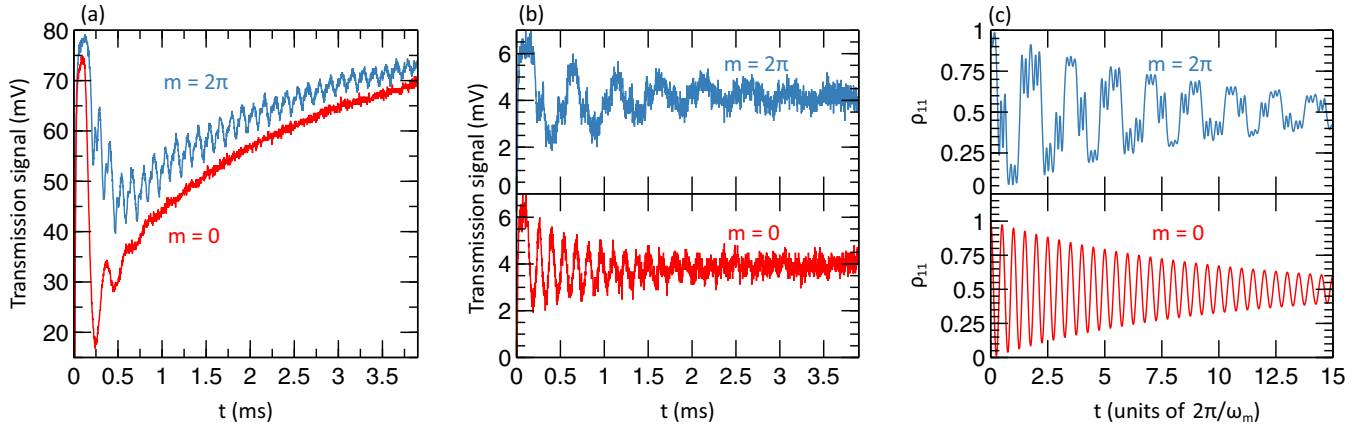
FIG. 9. (a, b) Influence of the probe's power on the double resonance signal in the case of a phase-modulated (blue) and unmodulated (red) driving MW field. Probe power is (a) 0.54 μW and (b) 0.06 μW. (c) Numerical simulation of a two-level system evolution in the case of small damping corresponding to (b), with simulation parameters $\Omega_R = 2\omega_m$, $\Gamma_1 = 2\Gamma_2 = 0.02\omega_m$.

time is increased by adding a trapping potential, e.g., an optical dipole trap. Another issue is that, due to the geometry of our experiment, it is hard to select a specific Zeeman transition by applying a bias magnetic field with a particular direction with respect to the polarization of the MW field. Again, in vapor-cell applications this problem usually is not present.

IV. CONCLUDING REMARKS

In summary, using double-resonance measurements in cold atoms, we have shown that the steady-state populations of two-level atoms interacting with a phase-modulated microwave field oscillate at multiples of the modulation frequency. We have applied the Rabi-resonance technique to cold atoms, and made the first observations of higher-order harmonics in any system. In the case when the carrier wave is exactly on resonance, we observe that only the even harmonics are present, which is confirmed by numerical solution of modified Maxwell-Bloch equations. Finally, we find that it is experimentally advantageous to use large optical probe powers in these measurements to damp "regular" Rabi oscillations and observe only the response to the modulation. These observations shed new light on the dynamics of a two-level system, which is currently a workhorse of many practical quantum information applications.

In addition, we have shown that the amplitude of the oscillations at $4\omega_m$ has a resonance when ω_m is varied. Our simulations show that at weak modulation the fourth harmonic has two resonance peaks: when $\Omega_R = 2\omega_m$ and $\Omega_R = 4\omega_m$.

The quartic dependence of the height of the latter peak and its smaller linewidth compared to that of the Rabi β resonance make a possible alternative for atomic-candle applications in experiments with a weak absorption signal, e.g., in cold atoms.

By exploring in depth the interactions between atoms and phase-modulated microwave fields, we have provided the foundations for a high signal-to-noise tool for measuring microwave fields, and thus the coupling to atomic systems. With the increasing use of three-dimensional microwave cavities [24,25], including with atomic systems [9], atomic-candle techniques can play an important role in calibrating the microwave field strengths for accurate measures of the coupling strength between the cavity field and, for instance, a microwave qubit [26–28]. These calibrations will be especially important for techniques that rely on precise timing, such as pulse-area-based quantum memories [29–31] and quantum transduction protocols [7,8,32,33].

ACKNOWLEDGMENTS

[1] T. Bandi *et al.*, *2012 IEEE International Frequency Control Symposium Proceedings, Baltimore, MD* (IEEE, New York, 2012), pp. 1–6.

[2] M. Pellaton *et al.*, Phys. Scr. T **149**, 014013 (2012).

[3] Y. Pétremand *et al.*, J. Micromech. Microeng. **22**, 025013 (2012).

[4] T. Bandi *et al.*, IEEE Trans. Ultrason. Ferroelectr. Freq. Control **61**, 1769 (2014).

[5] F. Y. Sun, D. Hou, Q. S. Bai, and X. H. Huang, J. Phys. Commun. **2**, 015008 (2018).

[6] A. Horsley and P. Treutlein, Appl. Phys. Lett. **108**, 211102 (2016).

[7] M. Hafezi, Z. Kim, S. L. Rolston, L. A. Orozco, B. L. Lev, and J. M. Taylor, Phys. Rev. A **85**, 020302 (2012).

[8] M. Kiffner *et al.*, New J. Phys. **18**, 093030 (2016).

[9] K. V. Adwaith, A. Karigowda, C. Manwatkar, F. Bretenaker, and A. Narayanan, Opt. Lett. **44**, 33 (2019).

[10] U. Cappeller and H. Müller, Ann. Phys. **497**, 250 (1985).

[11] J. C. Camparo, J. G. Coffer, and R. P. Frueholz, Phys. Rev. A **58**, 3873 (1998).

[12] J. C. Camparo, Phys. Rev. Lett. **80**, 222 (1998).

[13] J. G. Coffer, B. Sickmiller, A. Presser, and J. C. Camparo, Phys. Rev. A **66**, 023806 (2002).

[14] F. Sun *et al.*, Appl. Phys. Lett. **111**, 051103 (2017).

[15] M. Kinoshita, K. Shimaoka, and K. Komiyama, IEEE Trans. Instrum. Meas. **58**, 1114 (2009).

[16] M. Kinoshita, K. Shimaoka, and K. Komiyama, IEEE Trans. Instrum. Meas. **60**, 2696 (2011).

[17] M. Kinoshita, K. Shimaoka, and Y. Shimada, IEEE Trans. Instrum. Meas. **62**, 1807 (2013).

[18] T. Swan-Wood, J. Coffer, and J. Camparo, IEEE Trans. Instrum. Meas. **50**, 1229 (2001).

[19] X. Liu *et al.*, Rev. Sci. Instrum. **89**, 063104 (2018).

[20] H. Shi *et al.*, Sensors **18**, 3288 (2018).

[21] M. Kinoshita and M. Ishii, IEEE Trans. Instrum. Meas. **66**, 1592 (2017).

[22] H.-R. Noh and W. Jhe, Opt. Commun. **283**, 2353 (2010).

[23] A. V. Alekseev and N. V. Sushilov, Phys. Rev. A **46**, 351 (1992).

[24] M. Reagor *et al.*, Appl. Phys. Lett. **102**, 192604 (2013).

[25] F. Souris, H. Christiani, and J. P. Davis, Appl. Phys. Lett. **111**, 4 (2017).

[26] C. Grezes *et al.*, Phys. Rev. X **4**, 021049 (2014).

[27] D. Lachance-Quirion *et al.*, Sci. Adv. **3**, e1603150 (2017).

[28] A. P. Reed *et al.*, Nat. Phys. **13**, 1163 (2017).

[29] A. I. Lvovsky, B. C. Sanders, and W. Tittel, Nat. Photonics **3**, 706 (2009).

[30] C. Grezes *et al.*, C. R. Phys. **17**, 693 (2016).

[31] E. Saglamyurek *et al.*, Nat. Photonics **12**, 774 (2018).

[32] S. A. McGee, D. Meiser, C. A. Regal, K. W. Lehnert, and M. J. Holland, Phys. Rev. A **87**, 053818 (2013).

[33] R. W. Andrews *et al.*, Nat. Commun. **6**, 10021 (2015).